Nano Energy 103 (2022) 107785

Contents lists available at ScienceDirect

Nano Energy

journal homepage: www.elsevier.com/locate/nanoen

Highly transparent and water-repellent hierarchical-wrinkled-architecture triboelectric nanogenerator with ultrathin plasma-polymer-fluorocarbon film for artificial triboelectric skin

Eunmi Cho [a,c,1], Kyeong Nam Kim [b,1], Hyungseok Yong [a,1], Woo Jin Choi [a], Jin-Seong Park [c], Sang-Jin Lee [a,*]

[a] Chemical Materials Solutions Center, Korea Research Institute of Chemical Technology (KRICT), Daejeon 34114, the Republic of Korea
[b] Division of Energy Technology, DGIST, Daegu 42988, the Republic of Korea
[c] Department of Materials Science and Engineering, Hanyang University, Seoul 04763, the Republic of Korea

ARTICLE INFO

Keywords:
Hierarchical wrinkle
Plasma-polymer-fluorocarbon
Triboelectric nanogenerators
Raindrops energy harvester
Triboelectric skin

ABSTRACT

For scavenging energy from various places on the human body, multifunctional and comfortable triboelectric nanogenerators (TENG), that do not stimulate sensitive skin, are required. Therefore, it is essential to fabricate a TENG that is easy to deformation as well as biocompatible, ultrathin, and flexible. In this regard, we propose a hierarchical-wrinkled-architecture-TENG (HWA-TENG) with dual-wavelengths (microsize of 3.1 μm and nanosize of 311.8 nm). A plasma-polymer-fluorocarbon (PPFC) thin film was employed as a high-performance triboelectrification material, owing to its high surface charge potential, ultrathin thickness, transparency, and water repellency. The surface potential of the PPFC was extremely high at 7.28, which is comparable to that of bulk polytetrafluoroethylene. The surface area of HWA-TENG increased by as much as 3.5 % owing to the combination of the increased surface area effect of the HWA and high surface charge potential characteristics of the PPFC thin film, resulting in a high output performance of 200 V and 30 μA. The HWA-TENG can be successfully applied to triboelectric raindrops energy harvester and conformal artificial triboelectric skin. Owing to its eco-friendly, straightforward fabrication process, and high output performance, HWA-TENG can be used in several applications, including conformal TENGs for human body.

1. Introduction

The development of Internet of Things (IoT) and increasing interest in human health has triggered the production of a variety of sensors to measure various signals from the human body. However, the lack of a power source to drive these sensors and the absence of a battery for storage hamper the practical use of human body sensors. However, with the invention of triboelectric nanogenerators (TENG) that enable scavenging the electrical energy from a wide variety of places, it is possible to convert mechanical energy generated from the body movement to electrical energy. As an alternative to fossil fuels and for realizing carbon neutrality, energy from nature, such as solar, wind, and tidal power, is now converted to electrical energy and exploited. Moreover, energy can be continuously harvested from the daily activities of the human body and converted into electricity [1].

A TENG is a mechanical energy-harvesting device that uses the coupling of contact electrification and electrostatic induction. The several advantages of this technology, such as high efficiency, low cost, low density, light weight, and diverse choice of materials at low frequency make TENG superior to conventional electromagnetic, electrostatic, and piezoelectric-based biomechanical energy-harvesting technologies [2]. The technology that efficiently converts small amounts of energy from human motion into electricity has been extended to obtain energy from various available energy sources such as wind, water waves, water droplets, sound, magnetically induced motion, and keyboard typing [3–5]. The TENG is classified into four modes: contact-separation, lateral sliding, single-electrode, and freestanding triboelectric layer mode. Using these modes, various applications, including self-powered sensors, tactile and pressure sensors, audio sensors, and chemical sensors for artificial intelligence, have been

* Corresponding author.
E-mail address: leesj@krict.re.kr (S.-J. Lee).
[1] These authors contributed equally to this work.

https://doi.org/10.1016/j.nanoen.2022.107785
Received 26 June 2022; Received in revised form 26 August 2022; Accepted 6 September 2022
Available online 8 September 2022
2211-2855/© 2022 The Authors. Published by Elsevier Ltd. This is an open access article under the CC BY license (http://creativecommons.org/licenses/by/4.0/).

developed [3,6]. Particularly, monitoring of the complex human physiological signals with high sensitivity and sensation imitating the human touch has been reported [7]. Moreover, TENG-based sports sensing systems are leading to breakthrough progresses in the field of intelligent sports [2].

Extensive research has been conducted to improve the performance of TENG, and technology development strategies have been established. The key strategy involves the energy harvesting efficiency (EHE), which refers to the ratio of harvested electrical energy to the input mechanical energy. To improve the EHE, electrostatic force enhancement and displacement enhancement methods [8], nano-composite materials [9], multilayers [10,11], and matter-stimulations were adopted [12]. Among them, various methods for electrostatic force enhancement mainly involved the improvement of chemical surface modification (CSM) and physical surface modification (PSM). Particularly, CSM allows to charge of the surface to a well-charged surface through a modification or coating process. Polymer coatings are widely used for CSM, and Wang et al. [13]. investigated various triboelectric materials and proposed selection rules for various modes of TENG. Among them, polytetrafluoroethylene (PTFE) is a representative triboelectrification material that is mostly used in TENG for energy harvesting and sensing devices. Additionally, the good chemical and thermal resistance, low coefficient of friction, and biocompatibility allow it to be used for a variety of applications in TENG devices. However, the low flexibility due to its thickness, difficulty in adhering to a substrate due to its low surface energy, and low transparency due to haze limit its applications in various devices. Additionally, the use of PSM for EHE enhancement involves an increase in the surface area through patterning by lithography [14,15], plasma etching [16,17], and a combination of chemical treatment and mechanical stretching to create a wrinkled surface on the substrate [18,19].

In this study, we propose a hierarchical wrinkled architecture (HWA)-TENG that combines the CSM and PSM strategies. A plasma-polymer-fluorocarbon (PPFC) thin film was introduced as the high-performance triboelectrification material. A PPFC is a thin film with an amorphous structure produced by sputtering a composite target made by mixing PTFE and carbon nanotubes (CNTs) to impart electrical conductivity to the polymer targets. The features responsible for its

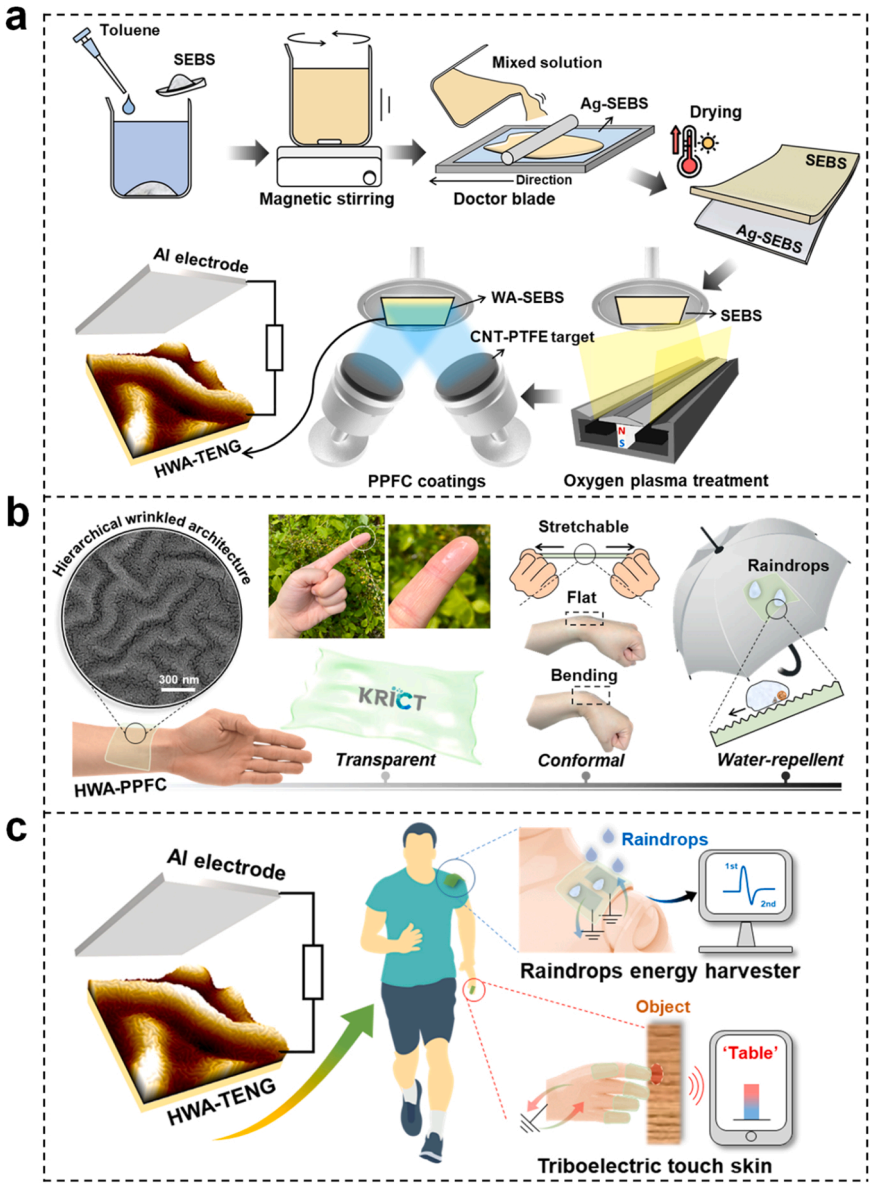

Fig. 1. (a) Schematic for the preparation of the HWA-PPFC based TENG (HWA-TENG). (b) Characteristics of the HWA-PPFC. (c) Application of the HWA-TENG based triboelectric raindrops energy harvester and touch skin.

suitability as triboelectrification material are surface charge density, limited thickness, low refractive index, water repellency, and biocompatibility. Additionally, sputtering is a clean process because it does not need hazardous gases used to produce conventional fluorocarbons, such as CF_4 or C_4F_8, with a high global warming potential index; therefore, it is an eco-friendly and future-oriented material in view of the carbon-neutral era. Biocompatible, stretchable, and transparent styrene-ethylene-butylene-styrene (SEBS) was used as the substrate of PPFC coated HWA-TENG. When the PPFC thin film was coated on the SEBS substrate, a nano-wrinkled structure concurrently formed on the surface. The CSM effect of the PPFC thin film and the PSM effect of the wrinkles appeared simultaneously. With the use of an additional oxygen plasma treatment, a hierarchical wrinkled architecture with dual wavelength is implemented, resulting in an enlarged surface area. The HWA-TENG exhibited a suitable performance as a body-mounted energy-harvesting device that requires high output in a small area because of the excellent triboelectrification characteristics of the PPFC and the improved surface area by dual-wavelength wrinkles. This HWA-TENG exhibited a surface engineering-enhanced output performance (voltage and current of 200 V and 30 μA, respectively) as well as outstanding mechanical stability (10,000 bending cycles) and long-term stability (2 h).

The HWA film also showed outstanding transparent, superhydrophobic, and conformal properties. Furthermore, we prepared transparent triboelectric raindrop sensors and conformal artificial triboelectric skin using the HWA-TENG. Their universal characteristics can be exploited in various industries, such as smart clothing, robots, and artificial skin for wearable applications. Fig. 1 shows the conceptual diagram of the study. The fabrication process of substrates with PPFC-coated hierarchical wrinkled architecture (HWA-PPFC) is shown in Fig. 1**a**, and the characteristics of HWA-PPFC, such as water repellency, transparency, conformability, and biocompatibility, are shown in Fig. 1**b**. Fig. 1**c** shows the applications of HWA-TENG as a raindrops-energy-harvester and conformal artificial triboelectric skin, which can be applied to the human body.

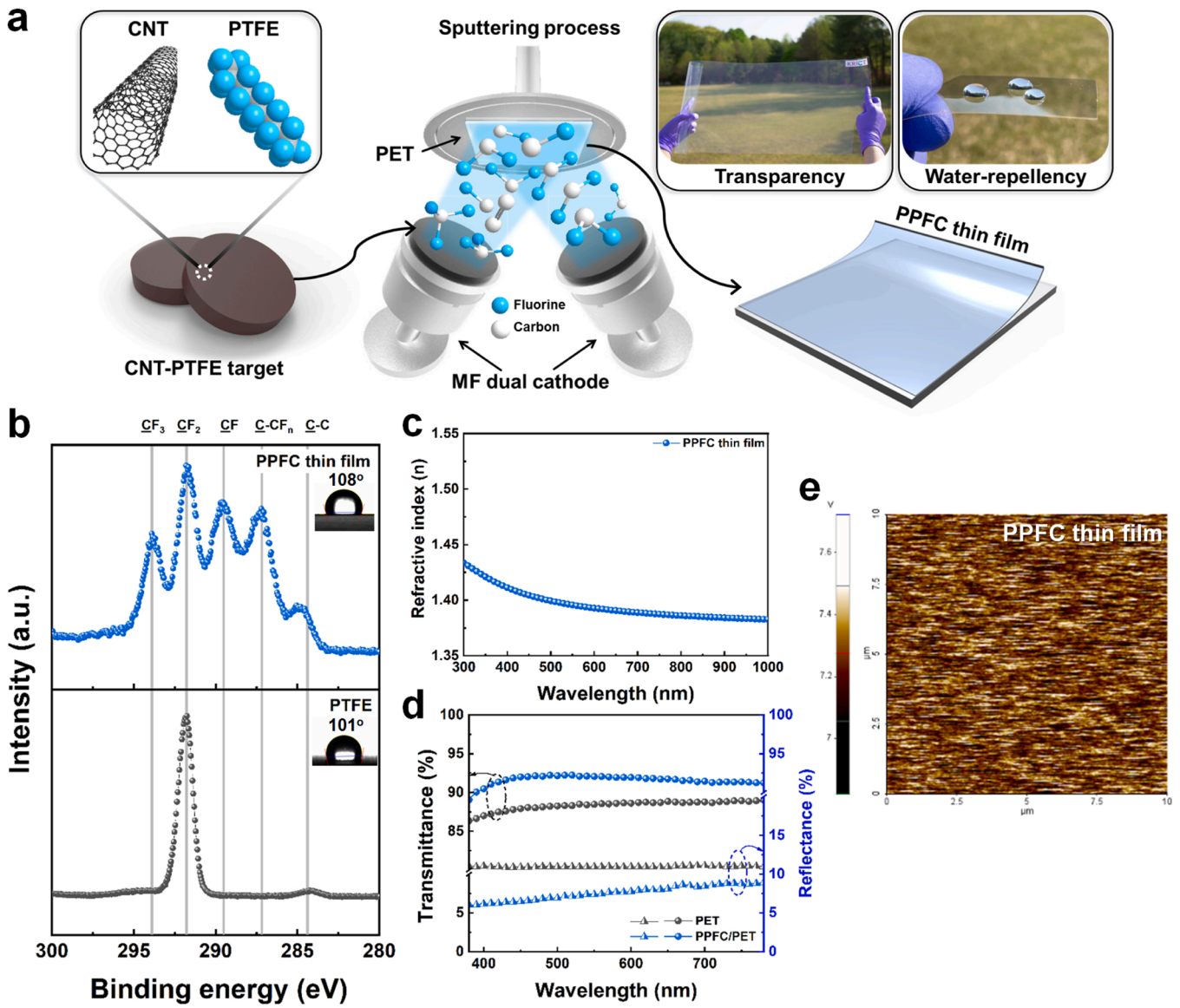

Fig. 2. Fabrication process and characteristics of the PPFC thin film. (a) Schematic of the PPFC thin film deposition process. (b) C 1*s* XPS spectra of PPFC and PTFE (the inset, shows the WCA of PPFC and PTFE). (c) Correlation between refractive index and wavelength. (d) Transmittance and reflectance spectra. (e) Surface charge potential of PPFC thin film using KPFM.

2. Results and discussion

2.1. Characteristics of PPFC thin film

A PPFC thin film fabricated by sputtering using a CNT–PTFE composite target exhibits properties similar to those of PTFE, such as hydrophobicity, electrical insulation, and chemical resistance. Furthermore, the PPFC thin film showed excellent adhesion to the substrate, good uniformity of nanometer-level thickness, smooth surface, and high transparency in the visible light region. Additionally, PPFC thin films can be manufactured on large-area substrates using a mid-range frequency (MF) sputtering system; by controlling the process conditions, the amount of fluorine and carbon in the thin film can be adjusted to tailor the thin-film properties.

Fig. 2 shows the unique characteristics of PPFC compared to that of PTFE. The PTFE exhibited a semi-crystalline structure with $–[-CF_2-CF_2-]_n–$ bonds, whereas PPFC thin films were randomly deposited on the substrate by the decomposition and recombination of carbon and fluorine atoms (or molecules) during the sputtering process (Fig. 2**a**). Consequently, the PPFC thin film had an amorphous structure. Additionally, during the sputtering process, CNT itself is not included in the PPFC, but is decomposed by carbon and recombined with fluorine to form a fluorocarbon. The X-ray photoelectron spectroscopy (XPS) analysis of the PPFC thin film showed the peaks for CF_3, CF, and $C—CF_n$ bonds in addition to those for CF_2 bonds, contrarily to the PTFE pattern which exhibited peaks for only CF_2 bonds (Fig. 2**b**). The CF_3 bond in the PPFC thin film had a surface energy of 15×10^{-3} N m^{-1}, which is much lower than that of the CF_2 bond (23×10^{-3} N m^{-1}) [20]. The water contact angle (WCA) of PPFC (108°), indicated a hydrophobic surface, and was higher than that of PTFE (WCA: 101°). Moreover, the low refractive index (1.38) of the PPFC thin film enhanced the optical properties of the transparent substrate (Fig. 2**c**) [21]. As shown in Fig. 2**d**, after coating the PPFC thin film (thickness: 100 nm) on the polyethylene terephthalate (PET) substrate, the transmittance increased by 3.6 % from 88.5 % to 92.1 %, and the reflectance decreased by 3.5%p from 10.9 % to 7.4 % at 550 nm wavelength. Furthermore, no additional absorption was observed for PPFC thin film in the visible region (Fig. S1). This result was due to the low refractive index minimizing the reflection by destructive interference between reflected waves, resulting in index matching that improved the PPFC thin film transmittance. Finally, the surface potential of the PPFC thin film, which measured the contact potential difference (V_{CPD}) between the tip and the sample using kelvin probe force microscopy (KPFM), was very high (7.28 V), similar to that of PTFE (Fig. 2**e**) [22].

2.2. Wrinkled architecture with the PPFC thin film coating

Fig. 3 shows the fabrication process of a wrinkled architecture with PPFC thin films (WA-PPFC) on the SEBS substrate and the surface morphological and optical properties. As shown in Fig. S2, a constant peak for CF^- (indicated by blue color) is observed for the PPFC thin film layer, which exists even on top of the SEBS layer, and gradually

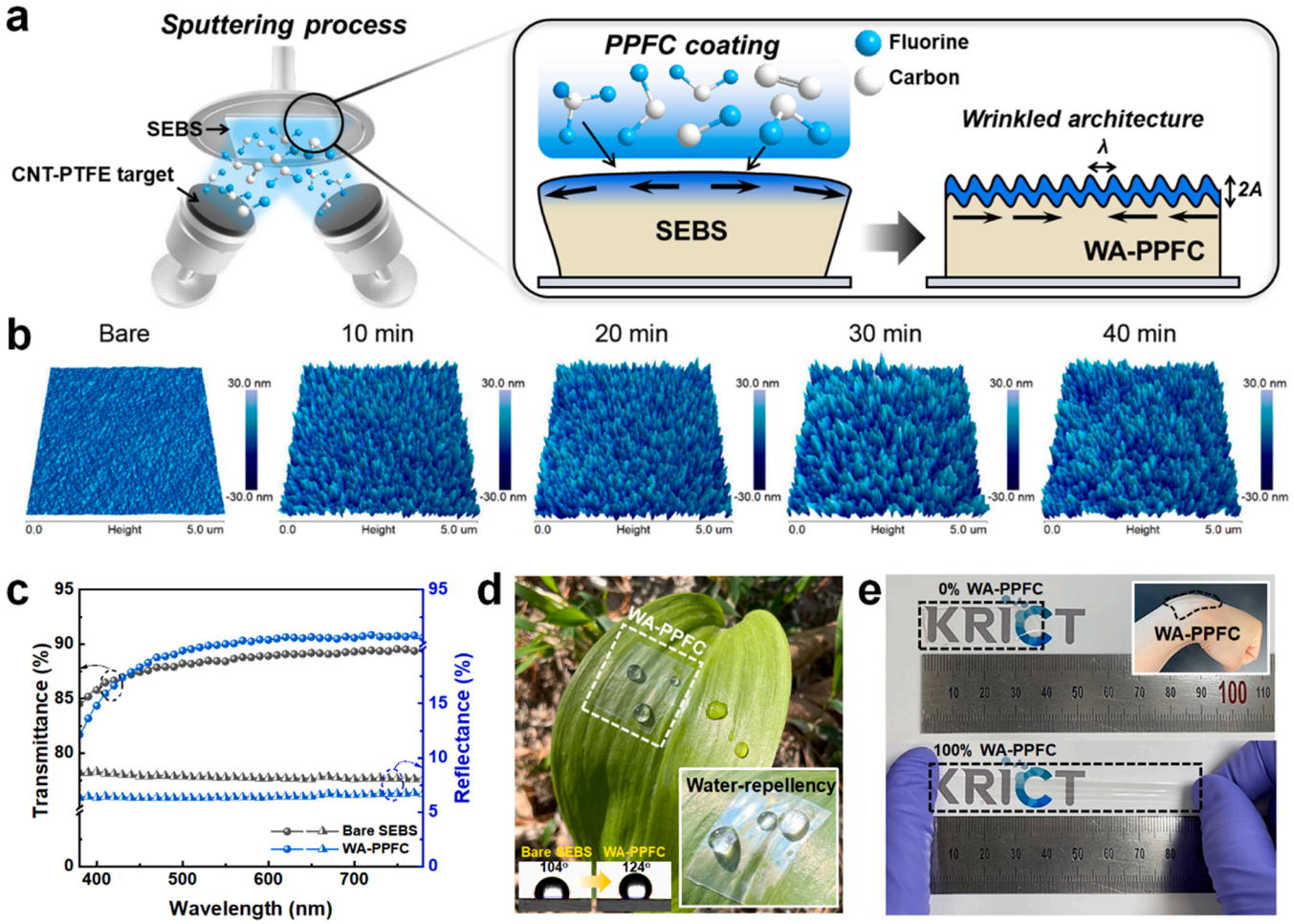

Fig. 3. Characteristics of WA-PPFC formed by PPFC thin film deposition process. (a) Illustration of the fabrication process of WA-PPFC. (b) Surface morphologies of WA-PPFC according to deposition time. (c) Transmittance and reflectance spectra of SEBS and WA-PPFC. (d) Photographs demonstrating the water-repellency and transparency of WA-PPFC. (e) Photographs of the stretchable and biocompatible WA-PPFC.

disappears in the SEBS substrate. This indicates that the F and C atoms from the CNT–PTFE composite target penetrated the SEBS substrate during the sputtering process. The SEBS can easily be penetrated by fluorocarbon, resulting in the formation of wrinkled architectures by volume expansion and deformation on the surface of the SEBS substrate (Fig. 3**a**) [23]. According to the linear elastic buckling theory, the wrinkling wavelength (λ) was calculated using Eq. (1) [24,25]:

$$\lambda = 2\pi h_f \left(\frac{(1-\nu_s^2)E_f}{3(1-\nu_f^2)E_s} \right)^{1/3} \quad (1)$$

where λ is the wrinkle wavelength, h_f is the thickness of the thin film, ν is Poisson's ratio, and E is Young's modulus. The subscripts f and s refer to the thin film and substrate, respectively. Poisson's ratios of a PPFC thin film (approximately Poisson's ratio for PTFE) and SEBS were approximately 0.46 and 0.49, respectively. Young's modulus of the PPFC thin film and SEBS were approximately 9.9 GPa and 1.4 MPa, respectively [26–28].

To analyze λ and the amplitude (2 A) of the wrinkled architectures in the WA-PPFC, the atomic force microscopy (AFM) images were analyzed using an image analysis software. The bare SEBS surface was flat and smooth; however, upon coating the PPFC thin film, nanoscale wrinkles

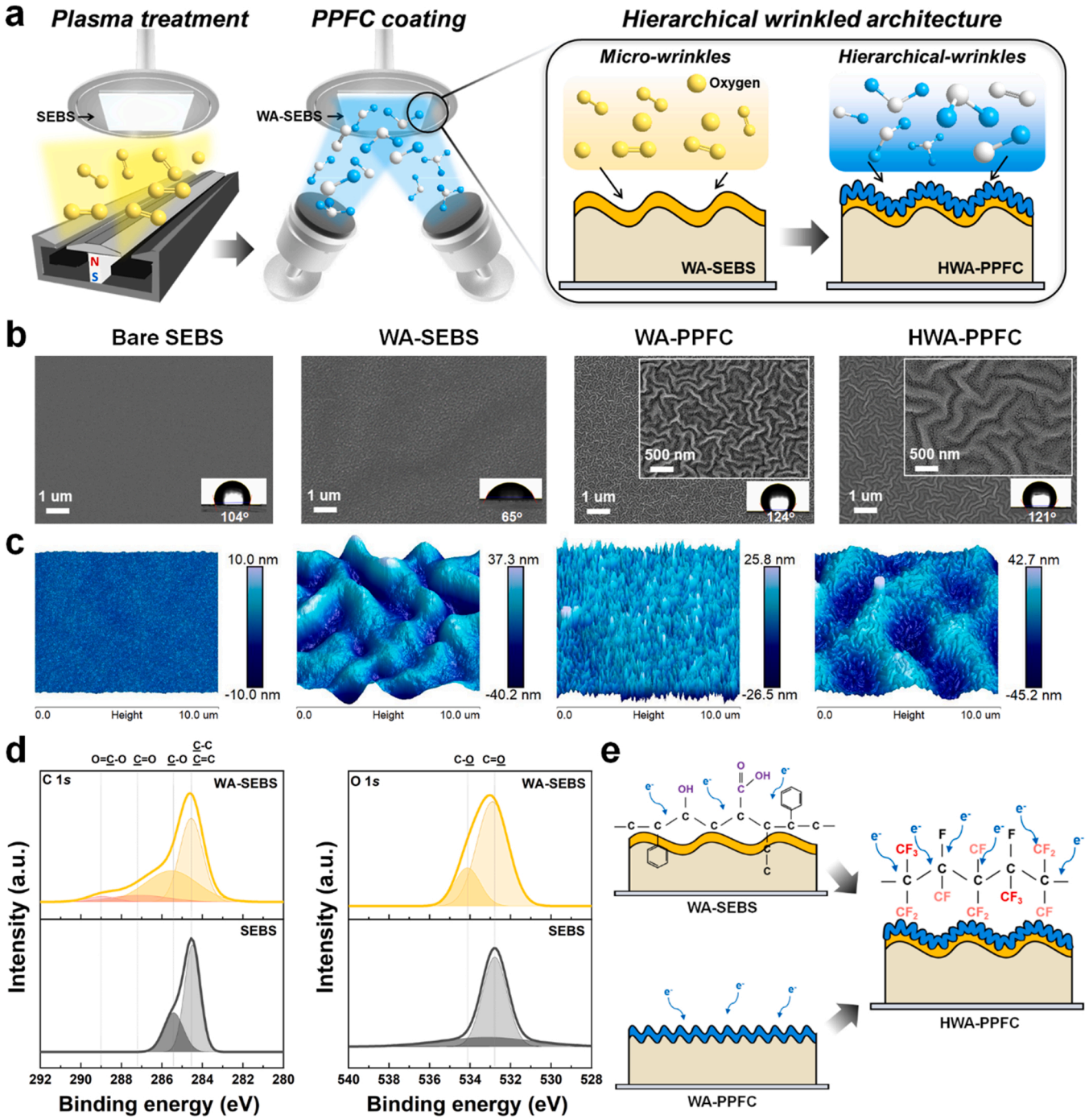

Fig. 4. (a) Illustration of the hierarchical wrinkled architecture formation. (b) Fe-SEM and (c) AFM images of SEBS, WA-SEBS, WA-PPFC and HWA-PPFC (the inset, shows the WCA images). (d) XPS spectra of C 1*s* and O 1*s* collected from bare SEBS and WA-SEBS (O_2). (e) Mechanism of enhanced triboelectric characteristic during each process of HWA-PPFC.

were formed (Fig. 3**b**). The sectional profile confirmed that as the deposition time increased, the wavelength of the wrinkles and the surface roughness (root mean square, RMS) increased. Consequently, the surface area of WA-PPFC increased by up to 2.72 %. The amplitude and wavelength of the WA-PPFC coated with the PPFC thin film for 30 min were 19.0 and 189.4 nm, respectively, and the RMS value was 8.93 nm (Fig. S3 and Table S1). These results were reasonably explained considering that C and F atoms or molecules penetrate the soft SEBS to form nano-wrinkles, owing to the volume expansion and deformation of elastic properties on the SEBS surface. However, upon PPFC coating for 40 min, the amplitude of the wrinkles decreased to 12.6 nm and the surface area difference decreased to 1.80 %, because fluorocarbon penetration was hampered by the stiff layer of SEBS during the sputtering process [29]. Therefore, the PPFC thin film was deposited on the surface of the stiff layer of the SEBS and gradually covered the already formed nano-wrinkles, decreasing of the amplitude and surface area of WA-PPFC. The surface area of the WA-PPFC reached a maximum at 30 min.

The optical properties of WA-PPFC improved because of the gradient refractive index effect of the nano-wrinkles and the low refractive index of the PPFC thin film [30]. As shown in Fig. 3**c**, the transmittance and reflectance of bare SEBS at 550 nm wavelengths were 88.4 % and 8.2 %, respectively, whereas the transmittance of WA-PPFC increased to 90.0 % and the reflectance decreased to 6.4 %. Fig. 3**d** shows photographs of the transparent and high water-repellent WA-PPFC. Because of the low surface energy of the PPFC thin film and the nano-wrinkles on the surface, the WCA of WA-PPFC improved to 124° from 104° for the bare SEBS. Moreover, Fig. 3**e** confirm that WA-PPFC retained the stretchable and biocompatible features of the SEBS substrate.

2.3. Hierarchical wrinkled architecture with PPFC via plasma process

To further improve the EHE by increasing the surface area of the WA-PPFC, a hierarchical wrinkled architecture with dual wavelength (microscale and nanoscale) was fabricated [31,32]. The substrates with HWA-PPFC were fabricated by plasma treatment using a linear ion source to the SEBS surface to make micro-wrinkles and coating them with PPFC to make nano-wrinkles by sputtering (Fig. 4**a**). Fig. 4**b** and **c** show the surface morphological changes of the samples observed using field-emission scanning electron microscopy (Fe-SEM) and AFM, respectively. A flat surface was observed in the bare SEBS, whereas a microscale-wrinkled architecture formed on the surface of the SEBS treated with oxygen plasma using a linear ion beam source (WA-SEBS). When plasma was applied to soft SEBS, ions with high energy penetrated the SEBS surface, and the surface layer was stiffened. Consequently, microscale wrinkles formed owing to the difference in strain between the newly formed stiff layer and SEBS substrate. The size of this wrinkle differed depending on the type of plasma process gas used. The WA-SEBS treated with oxygen and nitrogen plasma formed wrinkles with a larger amplitude and wavelength than the WA-SEBS treated with argon (Fig. S4). The AFM analysis of WA-SEBS showed that the amplitudes of wrinkles were 26.5 nm (Ar), 43.5 nm (O_2), and 40.5 nm (N_2), depending on the process gas. The wavelength of the wrinkle had a microscale of 1.8 μm (Ar), 3.0 μm (O_2), and 3.1 μm (N_2), respectively (Fig. S5 and Table S2). The reason for the different wrinkle sizes was the anode voltage applied to the active ions. In the plasma surface treatment process, the power was fixed at 10 W and the gas flow rate was 60 sccm; however, the anode voltages for each gas were 540 V (N_2), 513 V (O_2), and 452 V (Ar) (Table S2). The value of the anode voltage applied to the active ions was the energy transfer rate. The Ar, N_2, and O_2 gases incident on the SEBS surface transferred energy to the SEBS medium through collision energy transfer, which gradually decreased as the maximum energy at the surface penetrated the SEBS. In this process, a stiff layer (h_f) formed on the surface, and the energy transfer rate at the surface gradually decreased. In this case, the larger the anode voltage, the better the collision energy transfer. Therefore, oxygen and nitrogen gases, which have higher anode voltage values than that of argon, penetrated deeper, leading to wrinkles with relatively wide wavelength and amplitude, according to **Eq.** [33].

Additionally, the surface energy increased due to the plasma treatment, which modified the SEBS surface into a hydrophilic surface (Fig. S6). Particularly, when oxygen gas was used, hydroxyl groups (OH^-) and other oxygen functional groups were generated on the surface of SEBS, decreasing the WCA to 65°. Fig. 4**d** shows the XPS analysis results of SEBS and WA-SEBS (O_2). The oxygen-containing groups formed on the surface of WA-SEBS indicated that the oxygen plasma oxidized the alkyl ($–CH_3$) group to generate more oxygen-containing groups on the WA-SEBS (O_2); consequently, the oxidized WA-SEBS surface attracted electrons more easily to improve the triboelectrical performance [7].

By coating the PPFC thin film onto WA-SEBS, HWA-PPFC with micro-wrinkles and nano-wrinkles was fabricated. The SEM analysis revealed that the wrinkle dimension of HWA-PPFC was smaller than that of WA-SEBS and larger than that of WA-PPFC (Fig. 4**b**). Upon PPFC coating and modification of elastic properties by the oxygen plasma treatment, fluorocarbon penetrated the relatively hard surface of the SEBS. Therefore, because of the further change in the elastic properties of the substrate surface, nano-wrinkles with a wider wavelength than that of the WA-PPFC formed on the HWA-PPFC. Consequently, the WCA of the HWA-PPFC (121°) was smaller than that of the WA-PPFC (124°). The AFM image of HWA-PPFC shows that a hierarchical wrinkled architecture combined with micro- and nano-sized wrinkles was generated (Fig. 4**c**). The microsize wrinkle was the first generated wrinkle (G1), with wavelength and amplitude of 3.1 μm and 47.6 nm, respectively. The nanosize wrinkle was the wrinkle generated at the end (G2), with wavelength and amplitude of 311.8 and 12.7 nm, respectively. Moreover, the surface area of HWA-PPFC increased by as much as 3.5 % compared with 0.1 % increase in case of WA-SEBS and 2.7 % increase in case of WA-PPFC (Fig. S7 and Table S3). Accordingly, an HWA in which the microscale and nanoscale were combined was successfully formed through a sequential process of plasma surface treatment and PPFC thin film deposition, thereby increasing the surface area.

Fig. 4**e** shows the surface area of each sample and the effect of chemical bonding on the triboelectric potential. Oxygen-plasma-treated WA-SEBS attracted electrons via the OH^- functional groups, and the surface area increased due to the micro-wrinkles. Additionally, WA-PPFC attracted electrons more easily via functional groups containing F, and the surface area increased due to nano-wrinkles. Finally, the HWA-PPFC collected negative charges more easily because of the hierarchical wrinkled architecture (surface area increase of 3.5 %) and the PPFC thin film. Therefore, the high performance of the HWA-PPFC-based TENG (HWA-TENG) was explained by its flexibility, transparency, high water repellency and its excellent surface charge potential.

2.4. Characterizing the output and stability of HWA-TENG

Before the systematic characterization of the HWA-TENG, Fig. 5**a** shows the sequential operation mechanism depending on the contact and separation states. The initial state was the complete separation of the top and bottom parts, resulting in no charge transfer (Fig. 5**a**-(i)). Both surfaces were in the maximum level of contact in the pressed state, resulting in charge transfer, which was contact electrification (Fig. 5**a**-(ii)). In the releasing state, electrons moved from the bottom electrode to the top electrode through an external conductive path, because the negative charges in the bottom contact material repelled the electrons inside the neighboring electrode (Fig. 5**a**-(iii)). When the two surfaces were fully separated, they reached an equilibrium state, showing no electron flow to finish moving the electrons (Fig. 5**a**-(iv)). As the two surfaces were close, electrons moved back to the bottom electrodes owing to the attraction–repulsion transition (Fig. 5**a**-(v)).

Furthermore, the hierarchical wrinkled architecture enhanced the

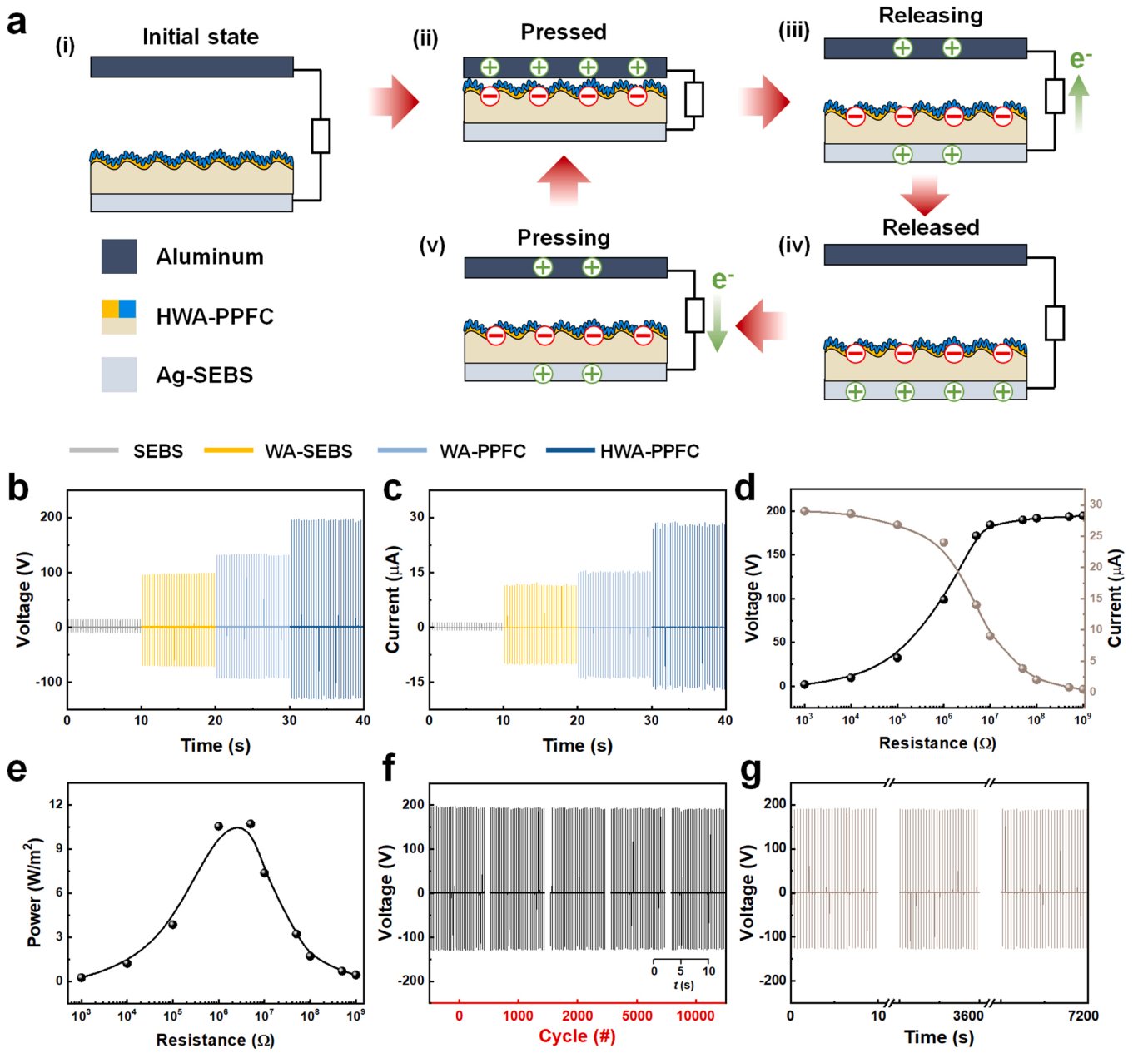

Fig. 5. Triboelectric nanogenerator device performance of HWA-TENG. (a) Operating mechanism of TENG. Comparison between (b) open-circuit voltages (V_{OC}) and (c) short-circuit currents (I_{SC}) of four different TENGs. (d) V_{OC} and I_{SC} curves with various outer resistance and (e) instantaneous power density derived from (d). (f) Mechanical stability of HWA-TENG under repeated bending motions (10,000 cycles) and (g) long-term reliability test under continuous vertical contact motion (for 2 h).

output generation performance of the TENG. As shown in Fig. 5**b** and **c**, the output signals of the TENGs with four friction layers were systematically measured and compared under contact motion with identical force (30 N) and frequency (3 Hz). Although the SEBS showed no output signals for energy harvesting, the HWA-PPFC exhibited a relatively high output voltage and current. The difference in output performance of the layers resulted from their surface area and electronegativity. Because the O_2 plasma generated a microwrinkle structure on the surface of the WA-SEBS, the output signals (100 V and 11 μA) were higher than those with the SEBS layer only. As the hydroxyl group (OH^-) was functionalized on the surface, the electronegativity of the layer also increased. The deposition of PPFC formed a nano-wrinkled structure on WA-PPFC and increased its electronegativity, resulting in a higher output performance (140 V, 15 μA). A further increase in the contact area of the layers from the hierarchical wrinkled architecture enhanced the triboelectric output performance of the TENG (200 V, 30 μA). The difference in the output performance of WA-SEBS, WA-PPFC, and HWA-PPFC suggested that many electrons were facilely transferred to the rough surface with abundant fluoride ions under contact and separation, as shown in Fig. 4**e** and following Eq. (2) [34].

$$Q_{SC} = \frac{S\sigma_c x}{\frac{d_1 \varepsilon_0}{\varepsilon_1} + x} \tag{2}$$

Where Q is the charge density, S is the surface area, σ_c is the surface charge density, x is the air-gap distance, d_1 is the thickness of the dielectric layer, ε_0 is the vacuum permittivity, and ε_1 is the dielectric constant of the insulator. In addition, the effect of the hierarchical wrinkled architecture on the output performance of TENG was confirmed through electrostatic simulation (Fig. S8). To reduce

distortion of mesh formation, the hierarchical structure was implemented as a large triangle with a height of 25 μm and a small triangle (two on the edge of large triangle) with a height of 3.535 μm. In this case, the potential of the hierarchical-triboelectric layer dramatically increased when the contact roughness was increased, which means that a higher charge density is generated on the hierarchical surface than on the surfaces of flat and wrinkle. Considering that an increase in charge density is directly related to an increase in transferred charge and a larger potential difference between electrodes, the distinguished electrical performance of HWA-TENG is closely related to the formation of the hierarchical structure (detailed in Supporting information).

The output characteristics of the TENG with hierarchical wrinkled architecture were further demonstrated by measuring the instantaneous power of the device, as shown in Fig. 5**d** and **e**. The output voltages and currents exhibited typical curves with increasing resistance. With an increase in the outer resistance, a decrease in the output current and an increase in the output voltage occurred. As derived from the curves of the output voltage and current, the instantaneous power density showed a maximum value of 11 W m^{-2} at a resistance of 10 MΩ. Accordingly, we compared with other literatures in power density as shown in Table S4 that this HWA-TENG produces one of the highest power density TENG based on PTFE film [35–51]. To confirm the feasibility of our HWA-TENG in wearable applications, we evaluated the bending stability (10,000 cycles, the radius of 4 mm, and the frequency of 1 Hz) and durability (2 h) of our TENG with a hierarchical wrinkled architecture, as shown in Fig. 5**f** and **g**. After 10,000 cycles of repeated bending motions (Video S1), the output voltage did not change, indicating a high mechanical stability. Durability tests (Video S2) indicated outstanding reliability under continuous long-term friction. In order to confirm the stability of the wrinkled HWA film against bending and continuous friction, we further characterized the surface morphology before and after bending/friction operations as shown in Fig. S9. It shows no visible damage or abrasion on the surface of film regardless of deformation. Thus, the stable output performances of HWA-TENG after bending and friction operation are attributed to excellent robustness under harsh environments.

Supplementary material related to this article can be found online at doi:10.1016/j.nanoen.2022.107785.

2.5. Energy harvesting applications of HWA-TENG

The main purpose of the HWA-TENG was to achieve high versatility and output as a triboelectric material. The HWA-TENG manufactured through multiple steps had a higher transparency than PTFE, which is most widely used as the triboelectric material, and had a similar output power to that of the solid–solid contact (Figs. 6**a** and S10a–b). Due to these characteristics, HWA-TENG exhibited high potential for utility and performance as a triboelectric material. With a TENG fabricated in 10 cm × 10 cm, SEBS (thickness: 50 μm) turned on approximately 30 LEDs, whereas PTFE (thickness: 100 μm) and HWA-TENG (PPFC thickness: 0.1 μm) both turned on approximately 100 LEDs with comparable brightness (Fig. 6**b** and Videos S3–5). In addition, to quantitatively compare the electrical outputs, a circuit containing a rectified TENG capable of charging a capacitor was prepared (Figs. 6**c–d** and S11a–b). For 100 s, the capacitor of 100 μF was charged to 0.2 V for SEBS, whereas the capacitor was charged to 1.2 V and 1.1 V for PTFE and HWA-TENG, respectively (Fig. S11c). Despite the difference in thickness between the HWA-TENG and PTFE, their outputs were analogous. Additionally, the HWA-PPFC based TENG operated a small electronic device (humidity and temperature sensor) through a capacitor charged to 1000 μF (Fig. 6**e** and **f**, and Video S6). The output of HWA-PPFC based TENG was also confirmed under relative humidity conditions, considering an actual environment (Fig. S12). These results demonstrated that the HWA-TENG can be used as a triboelectric material with a surface charge density similar to that of PTFE.

Supplementary material related to this article can be found online at doi:10.1016/j.nanoen.2022.107785.

One of the applications of TENG is to harvest water energy by liquid–solid contact [52,53]. This application requires a specific environment in which light can be transmitted, such as a window [54] or a solar panel [55,56]. A liquid–solid contact-based TENG was produced to compare the energy production of each material by water droplets (Figs. 6**g** and S13). The two electrodes were connected in a freestanding mode, with one of the connection modes used in the TENG to collect energy from a fixed position [57]. Moreover, to analyze the electrical output power from the complex flow of water droplets, the voltage was measured at the electrode (Ψ1: upper electrode, Ψ2: bottom electrode) using an ungrounded method [58,59]. The mechanism of charge transfer through the contact electrification between liquid and solid surfaces is controversial, but recent studies have shown that electrons move from water molecules to solid surfaces, leading to negative charges [60,61]. Therefore, the water molecules become positively charged upon losing electrons, and the solid surface becomes negatively charged upon electron transfer. Therefore, the region separated from the liquid was characterized by a negative potential, owing to the remaining electrons, and the liquid had a positive potential, owing to the surplus cations (Fig. 6**h**). When the droplet reached the upper electrode (first shedding), the electrode was affected by the accumulated surplus cations; the potential of the upper electrode increased, and a free charge of the cathode was induced (positive voltage), as shown in Fig. 6**i** (1st). When the droplets reached the bottom electrode, the potential of the surplus cation affected both the electrodes (2nd). Therefore, when water droplets flowed along the surface, irregular non-sinusoidal energy was generated. Because PTFE and HWA-TENG had similar hydrophobicity and surface charge density, the output by water droplets was also analogous (Fig. S14a–d). This output was rectified using a rectifier to effectively turn on an LED (Figs. 6**j** and S14e). Considering the environment in which the liquid–solid contact-based TENG was utilized, the LED was fixed on the backside of each device. Owing to the comparable outputs, the brightness of the LEDs was similar; however, the HWA-TENG transmitted a larger amount of light than PTFE (Figs. 6**k**, S15, and Videos S7 and 8). These results show that the HWA-TENG can be used in applications that require transparency, such as windows and solar panels.

Supplementary material related to this article can be found online at doi:10.1016/j.nanoen.2022.107785.

Furthermore, a new concept of energy harvesting method using the human body as an energy transfer medium has been developed [62–65]. Although this method is not restricted to electrodes or wires, the limitations include installing them at specific locations or wearing specific clothing, such as shoe soles or gloves. Therefore, the development of a triboelectric skin with a high surface charge density minimizes the user discomfort. The biocompatibility and elasticity of the HWA-TENG substrate material make it suitable to be attached to human skin. Additionally, the HWA-TENG can be manufactured using ultrathin triboelectric skin, owing to the easily adjustable thickness. By attaching the triboelectric skin to the fingertips, the energy of contact electrification when touching an object can be converted into usable energy through the human body (Fig. 6**l**). The ultrathin triboelectric skin could be transparently attached to the actual fingertips (Fig. 6**m**). The electrical output from this triboelectric skin was analyzed for several materials used in daily life (Fig. 6**n**). When there was no triboelectric skin, an electrical output was not generated because there was no insulating layer. However, the triboelectric skin generated 1 V, 3 V, and more than 10 V of usable energy with table, angora, and metal tumbler, respectively (Fig. S16). These outputs occurred sequentially when the fingertips touched the object. The triboelectric skin using the HWA-TENG converts various physical activities of humans into usable energy in daily life through body-mediated energy transfer.

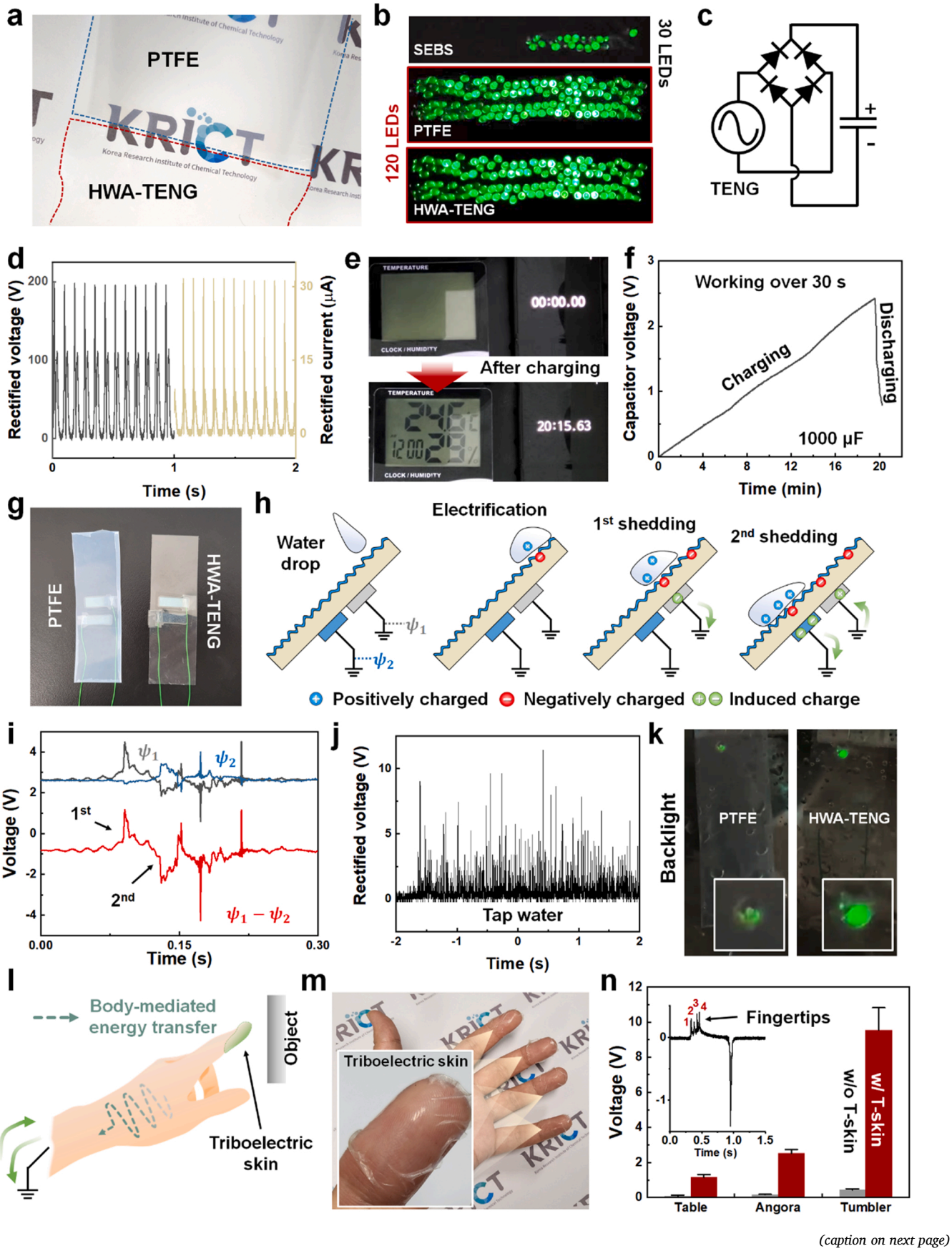

(caption on next page)

Fig. 6. Energy harvesting applications of HWA-TENG. (a) Photographs of HWA-TENG and PTFE. (b) Brightness of LEDs with TENG application (SEBS: 30 LEDs, PTFE: 120 LEDs, HWA-TENG: 120 LEDs). (c) Circuit diagram of TENG with full-bridge rectifier and capacitor. (d) Rectified voltage and current of HWA-TENG. (e) Photographs for the operation of the humidity and temperature sensor through HWA-TENG and (f) a charging voltage of the capacitor (1000 μF). (g) Photographs of liquid-solid contact-based TENG made of PTFE and HWA-PPFC. (h) Energy generation mechanism of liquid-solid contact-based TENG. (i) Induced voltage of electrodes measured using the non-grounded method. 1st: the droplet reaches the upper electrode; 2nd: the droplet flows over the bottom electrode. Ψ1 and Ψ2 denote the electrical potentials of upper and bottom electrodes, respectively. (j) Rectified voltage of liquid-solid contact-based TENG made of HWA-PPFC by tap water. (k) Brightness of LED passing through the PTFE and HWA-TENG. (l) Concept of body-mediated energy transfer with triboelectric skin. (m) Photographs of triboelectric skin made of HWA-TENG on fingertips. (n) Induced voltage of body-mediated energy transfer with triboelectric skin according to objects in daily life. The inset, shows a waveform of the voltage generated when each fingertip touches the objects sequentially.

3. Conclusions

The performance of PPFC thin film as a triboelectric material was proved to be suitable for small, compact, and conformal TENG devices. A wrinkled architecture was fabricated via a facile fabrication technique by coating PPFC on stretchable and biocompatible SEBS substrates, and an additional oxygen plasma treatment was employed to fabricate hierarchical wrinkled architecture. The HWA-PPFC exhibited a 3.5 % increase in surface area, which further enhanced its ability to attract negative charges combined with the PPFC thin film with a high surface potential. The HWA-TENG showed an output performance of 200 V and 30 μA, which was approximately 20 times higher than that without HWA. The transparent, stretchable, and water-repellent HWA-TENG exhibited an excellent performance when applied to various devices, such as LED lighting, humidity and temperature sensors, liquid–solid mode droplet tests, and triboelectric skin. Although the thickness of the PPFC thin film was 0.1 μm, which is 1000 times less than that of PTFE (100 μm), the two systems showed comparable TENG performances. Its potential and applicability were demonstrated by attaching a stretchable and biocompatible HWA-TENG to human fingers to realize a triboelectric skin. In conclusion, the HWA-TENG combined with PPFC thin films accelerate the realization of TENG as a power source for various inexpensive electronic devices, including sensors for human body attachment.

4. Experimental section

4.1. Materials

The SEBS resin was prepared by dissolving SEBS powder (Mirae Trading Company) in toluene (weight ratio, 4:10). Next, the SEBS film (20 μm) was coated on a PET (V7610, SKC, 100 μm) substrate using a micrometer applicator (Elcometer, Inc., Manchester, United Kingdom) and dried (60 °C for 10 min).

To prepare the PPFC thin film, multiwall CNT powder (K-nanos 200P, powder size 5–15 μm, Hanwha Chemical) and PTFE powder (TF-1750, powder size 25 μm, Dyneon) were first mixed in a weight ratio (5:95). The mixed powders were placed in a mold, pressed at 200 kg_f cm^{-2}, and heat-treated at 375 °C to prepare the CNT–PTFE composite target. The prepared composite target had the form of a disk of diameter 10.16 cm and thickness 6 mm.

The sputtering chamber was evacuated to a base pressure of 5.0×10^{-6} Torr using a mechanical pump and a cryogenic pump. Pure Ar gas was used as the sputtering gas and its flow rate was controlled at 8 mTorr using a mass flow controller. The PPFC thin films were fabricated by sputtering with a dual-cathode MF power supply (PE II, 40 kHz frequency, Advanced Energy) using a CNT–PTFE composite target. The target-to-substrate distance was maintained at 240 mm.

4.2. Fabrication of HWA-TENG

The back electrodes comprised the screen-printed silver electrodes for TENG characterization [66]. The printable silver ink was made of 3 g of silver flakes (Sigma-Aldrich, 10 μm) and 1.5 g of SEBS resin using a planetary paste mixer for 5 min at a speed of 2000 rpm. A SEBS film (20 μm) was coated on the electrode. The WA-TENG was fabricated by coating the PPFC thin films at 300 W for 10, 20, 30, and 40 min. The PPFC thin films were deposited simultaneously on the SEBS substrate and Si wafers, and the thickness was measured using an alpha-step method (DektakXT, Bruker). The HWA-TENG was prepared by plasma treatment with a linear ion source (LIS, LIS450, Advanced thin film) and deposition of PPFC thin films. The Ar, O_2, and N_2 gases were used for the plasma treatment. The gas flow rates were the same at 60 sccm. Plasma treatment was conducted using a direct current power supply (Forte I-302, EN Technologies Inc.) at 10 W, within a processing time of 1 min. Subsequently, a hierarchical wrinkled surface was prepared by depositing the PPFC thin film through sputtering. For the positive conductive layer, commercial aluminum tape (1.5 cm × 1.5 cm) was attached to the PET substrate. A resin-encapsulated conductive wire was exposed to fire ignition and connected to the top and bottom electrodes using stretchable silver ink.

For the application of solid–solid contact-based TENG, a large area of TENG (10 cm × 10 cm) was fabricated for effective output comparison with PTFE. Both the positive conductive layer and back electrode were composed of commercial aluminum tape and attached to a poly(methyl methacrylate) plate. A Teflon-wrapping conductive wire was connected to both electrodes. Additionally, triboelectric materials (SEBS 20 μm, PTFE 100 μm, and HWA-PPFC: 100 nm on SEBS) were attached to the side of the electrode.

In transparent TENG applications based on liquid–solid contacts, indium tin oxide (ITO) electrodes were used. To achieve a thickness comparable to that of the insulating layer, PET sheets (width: 30 mm, length: 100 mm, thickness: 100 μm) were used as substrates. Two ITO electrodes (width: 20 mm; length: 5 mm) were attached to the backside of the PET sheets. The front surfaces of the PET sheets were covered with PTFE film and HWA-PPFC.

For triboelectric skin applications, HWA-PPFC was sequentially fabricated on a release film (3 cm × 2 cm) for easy separation from the substrate. After the plasma process, the release film was peeled off and carefully placed on the fingertips to allow easy adherence to the skin. Fig. S17 shows that the WCA of HWA-PPFC maintains the same value before and after removal from the release film. This result suggests that the wrinkle surface remains unchanged before and after removal from the release film. To measure the energy converted through the human body, the oscilloscope probe was placed in contact with the fingertips of the opposite hand to which the triboelectric skin was attached.

4.3. Characterization and measurement

The wrinkled morphologies and profile structures were analyzed by Fe-SEM (MAIA3, TESCAN) and AFM (XE-100, Park Systems). The AFM was operated in the tapping mode with scan ranges of (5 μm × 5 μm) and (10 μm × 10 μm). Three-dimensional information and sectional profiles of the samples were obtained using the NanoScope Analysis software. The KPFM measurements were performed using a Park Systems (XE-100) with NSC14/Cr-Au cantilever tips (force constants 3 N m^{-1} and resonance frequency of 75 kHz). Depth profiling was performed using time-of-flight secondary ion mass spectrometry (ION-TOF M6, Germany), using a sputtering beam of O^{2+} at 1 keV raster-scanned over (500 μm × 500 μm), and an analysis beam of Bi^{3+} at 30 keV raster-scanned over (150 μm × 150 μm).

Chemical analysis of the samples was conducted using XPS (AXIS

NOVA, Kratos). The Al-Kα X-rays were used, and the acceleration voltage was 15 keV. The wavelength dependent refractive index of PPFC was analyzed using an ellipsometer (Elli-Se-Uam12, Ellipsotech). The WCA of the PPFC thin films was measured using a contact angle analyzer (PHOENIX 300 touch, Surface Electro Optics). The deionized water droplets were 5 μL in volume, and the measurement of WCA images of PPFC thin film were repeated three times. The optical properties were measured in the wavelength range 380–780 nm using an optical spectrometer (U-4100, Hitachi). Repeated vertical pressure was generated using a pushing tester (Labworks, ET-139 shaker, and PA-151 power amplifier). The voltage and current of the TENG were characterized using digital phosphor oscilloscopes (Tektronix, Inc., DPO 4054 B and MDO34) and a low-noise current preamplifier (Stanford Research Systems, Inc., SR570), respectively. The input contact force was measured using an oscilloscope connected to a force sensor (Dytran Instruments, Inc., 1053V3). The bending test was conducted using a bending tester (Junil Tech, JIRBT-620).

CRediT authorship contribution statement

Sang-Jin Lee conceived the idea and designed the experiments. Eunmi Cho and Jin-Seong Park conducted the plasma-polymer-fluorocarbon (PPFC) thin film and plasma treatment using linear ion source experiments and data analysis. Kyeong Nam Kim, Hyungseok Yong and Woo Jin Choi fabricated the TENG and analyzed the TENG characterization. Eunmi Cho, Kyeong Nam Kim, Hyungseok Yong and Sang-Jin Lee wrote the manuscript. All of the authors discussed the results and commented on the manuscript. All of the authors discussed the results and commented on the manuscript.

Declaration of Competing Interest

The authors declare that they have no known competing financial interests or personal relationships that could have appeared to influence the work reported in this paper.

Data Availability

Data will be made available on request.

Acknowledgements

This study was supported by the Core Research Project at Korea Research Institute of Chemical Technology (KRICT) (SI2252-20) funded by the Ministry of Science and ICT, Korea.

Appendix A. Supporting information

Supplementary data associated with this article can be found in the online version at doi:10.1016/j.nanoen.2022.107785.

References

[1] L. Yin, K.N. Kim, A. Trifonov, T. Podhajny, J. Wang, Designing wearable microgrids: towards autonomous sustainable on-body energy management, Energy Environ. Sci. 15 (2022) 82–101, https://doi.org/10.1039/D1EE03113A.
[2] J. Luo, W. Gao, Z.L. Wang, The triboelectric nanogenerator as an innovative technology toward intelligent sports, Adv. Mater. 33 (2021), 2004178, https://doi.org/10.1002/adma.202004178.
[3] W.-G. Kim, D.-W. Kim, I.-W. Tcho, J.-K. Kim, M.-S. Kim, Y.-K. Choi, Triboelectric nanogenerator: structure, mechanism, and applications, ACS Nano 15 (2021) 258–287, https://doi.org/10.1021/acsnano.0c09803.
[4] J.H. Lee, S. Kim, T.Y. Kim, U. Khan, S.-W. Kim, Water droplet-driven triboelectric nanogenerator with superhydrophobic surfaces, Nano Energy 58 (2019) 579–584, https://doi.org/10.1016/j.nanoen.2019.01.078.
[5] P. Maharjan, T. Bhatta, C. Park, H. Cho, K. Shrestha, S. Lee, M. Salauddin, M. Rahman, S.S. Rana, J.Y. Park, High-performance keyboard typing motion driven hybrid nanogenerator, Nano Energy 88 (2021), 106232, https://doi.org/10.1016/j.nanoen.2021.106232.
[6] D. Wang, D. Zhang, Y. Yang, Q. Mi, J. Zhang, L. Yu, Multifunctional latex/polytetrafluoroethylene-based triboelectric nanogenerator for self-powered organ-like MXene/metal–organic framework-derived CuO nanohybrid ammonia sensor, ACS Nano 15 (2021) 2911–2919, https://doi.org/10.1021/acsnano.0c09015.
[7] Y.-W. Cai, X.-N. Zhang, G.-G. Wang, G.-Z. Li, D.-Q. Zhao, N. Sun, F. Li, H.-Y. Zhang, J.-C. Han, Y. Yang, A flexible ultra-sensitive triboelectric tactile sensor of wrinkled PDMS/MXene composite films for E-skin, Nano Energy 81 (2021), 105663, https://doi.org/10.1016/j.nanoen.2020.105663.
[8] G. Zhu, J. Chen, T. Zhang, Q. Jing, Z.L. Wang, Radial-arrayed rotary electrification for high performance triboelectric generator, Nat. Commun. 5 (2014) 3426, https://doi.org/10.1038/ncomms4426.
[9] W. Seung, H.J. Yoon, T.Y. Kim, H. Ryu, J. Kim, J.-H. Lee, J.H. Lee, S. Kim, Y. K. Park, Y.J. Park, S.-W. Kim, Boosting power-generating performance of triboelectric nanogenerators via artificial control of ferroelectric polarization and dielectric properties, Adv. Energy Mater. 7 (2017), 1600988, https://doi.org/10.1002/aenm.201600988.
[10] N. Cui, L. Gu, Y. Lei, J. Liu, Y. Qin, X. Ma, Y. Hao, Z.L. Wang, Dynamic behavior of the triboelectric charges and structural optimization of the friction layer for a triboelectric nanogenerator, ACS Nano 10 (2016) 6131–6138, https://doi.org/10.1021/acsnano.6b02076.
[11] Z. Li, M. Zhu, Q. Qiu, J. Yu, B. Ding, Multilayered fiber-based triboelectric nanogenerator with high performance for biomechanical energy harvesting, Nano Energy 53 (2018) 726–733, https://doi.org/10.1016/j.nanoen.2018.09.039.
[12] B.U. Ye, S.Y. Lee, M. Jung, S.-D. Sohn, H.-J. Shin, M.H. Song, K.J. Choi, J.M. Baik, Photo-stimulated triboelectric generation, Nanoscale 9 (2017) 18597–18603, https://doi.org/10.1039/c7nr07020a.
[13] Z. Zhao, L. Zhou, S. Li, D. Liu, Y. Li, Y. Gao, Y. Liu, Y. Dai, J. Wang, Z.L. Wang, Selection rules of triboelectric materials for direct-current triboelectric nanogenerator, Nat. Commun. 12 (2021) 4686, https://doi.org/10.1038/s41467-021-25046-z.
[14] S. Li, J. Wang, W. Peng, L. Lin, Y. Zi, S. Wang, G. Zhang, Z.L. Wang, Sustainable energy source for wearable electronics based on multilayer elastomeric triboelectric nanogenerators, Adv. Energy Mater. 7 (2017), 1602832, https://doi.org/10.1002/aenm.201602832.
[15] D. Kim, S.-J. Park, S.-B. Jeon, M.-L. Seol, Y.-K. Choi, A triboelectric sponge fabricated from a cube sugar template by 3D soft lithography for superhydrophobicity and elasticity, Adv. Electron. Mater. 2 (2016), 1500331, https://doi.org/10.1002/aelm.201500331.
[16] L. Liu, W. Tang, Z.L. Wang, Inductively-coupled-plasma-induced electret enhancement for triboelectric nanogenerators, Nanotechnology 28 (2016), 035405, https://doi.org/10.1088/1361-6528/28/3/035405.
[17] X. Cheng, B. Meng, X. Chen, M. Han, H. Chen, Z. Su, M. Shi, H. Zhang, Single-step fluorocarbon plasma treatment-induced wrinkle structure for high-performance triboelectric nanogenerator, Small 12 (2016) 229–236, https://doi.org/10.1002/smll.201502720.
[18] Y. Feng, Y. Zheng, Z.U. Rahman, D. Wang, F. Zhou, W. Liu, Paper-based triboelectric nanogenerators and their application in self-powered anticorrosion and antifouling, J. Mater. Chem. A 4 (2016) 18022–18030, https://doi.org/10.1039/c6ta07288g.
[19] Y. Feng, Y. Zheng, S. Ma, D. Wang, F. Zhou, W. Liu, High output polypropylene nanowire array triboelectric nanogenerator through surface structural control and chemical modification, Nano Energy 19 (2016) 48–57, https://doi.org/10.1016/j.nanoen.2015.11.017.
[20] W.A. Zisman, Relation of the Equilibrium Contact Angle to Liquid and Solid Constitution, American Chemical Society, Washington, DC, 1964.
[21] S.H. Kim, C.H. Kim, W.J. Choi, T.G. Lee, S.K. Cho, Y.S. Yang, J.H. Lee, S.-J. Lee, Fluorocarbon thin films fabricated using carbon nanotube/polytetrafluoroethylene composite polymer targets via mid-frequency sputtering, Sci. Rep. 7 (2017) 1451, https://doi.org/10.1038/s41598-017-01472-2.
[22] S.S. Kwak, S. Lin, J.H. Lee, H. Ryu, T.Y. Kim, H. Zhong, H. Chen, S.-W. Kim, Triboelectrification-induced large electric power generation from a single moving droplet on graphene/polytetrafluoroethylene, ACS Nano 10 (2016) 7297–7302, https://doi.org/10.1021/acsnano.6b03032.
[23] S.-J. Yu, Y.-P. Du, Y.-D. Sun, Q.-L. Ye, H. Zhou, Wrinkling patterns in metal films sputter deposited on viscoelastic substrates, Thin Solid Films 638 (2017) 230–235, https://doi.org/10.1016/j.tsf.2017.07.051.
[24] J.Y. Chung, A.J. Nolte, C.M. Stafford, Surface wrinkling: a versatile platform for measuring thin-film properties, Adv. Mater. 23 (2011) 349–368, https://doi.org/10.1002/adma.201001759.
[25] B. Osmani, H. Deyhle, T. Töpper, T. Pfohl, B. Müller, Gold layers on elastomers near the critical stress regime, Adv. Mater. Technol. 2 (2017), 1700105, https://doi.org/10.1002/admt.201700105.
[26] P.J. Rae, E.N. Brown, The properties of poly(tetrafluoroethylene) (PTFE) in tension, Polymer 46 (2005) 8128–8140, https://doi.org/10.1016/j.polymer.2005.06.120.
[27] S.H. Kim, M. Kim, M.S. Um, W.J. Choi, J.H. Lee, Y.S. Yang, S.-J. Lee, Effects of carbon concentration on high-hardness plasma-polymer-fluorocarbon film deposited by mid-range frequency sputtering, Sci. Rep. 9 (2019) 10664, https://doi.org/10.1038/s41598-019-46993-0.
[28] H. Mae, M. Omiya, K. Kishimoto, Comparison of mechanical properties of PP/SEBS blends at intermediate and high strain rates with SiO_2 nanoparticles vs. $CaCO_3$ fillers, J. Appl. Polym. Sci. 110 (2008) 1145–1157, https://doi.org/10.1002/app.28724.
[29] E.S. Kim, S.H. Kim, S.-J. Lee, J.H. Lee, M. Byeon, D.H. Suh, W.J. Choi, Facile fabrication of micro/nano-structured wrinkles by controlling elastic properties of

polydimethylsiloxane substrates, Polymer 212 (2021), 123087, https://doi.org/10.1016/j.polymer.2020.123087.
[30] X. Liu, K. Cheng, P. Cui, H. Qi, H. Qin, G. Gu, W. Shang, S. Wang, G. Cheng, Z. Du, Hybrid energy harvester with bi-functional nano-wrinkled anti-reflective PDMS film for enhancing energies conversion from sunlight and raindrops, Nano Energy 66 (2019), 104188, https://doi.org/10.1016/j.nanoen.2019.104188.
[31] J. Ahn, Z.-J. Zhao, J. Choi, Y. Jeong, S. Hwang, J. Ko, J. Gu, S. Jeon, J. Park, M. Kang, D.V.D. Orbe, I. Cho, H. Kang, M. Bok, J.-H. Jeong, I. Park, Morphology-controllable wrinkled hierarchical structure and its application to superhydrophobic triboelectric nanogenerator, Nano Energy 85 (2021), 105978, https://doi.org/10.1016/j.nanoen.2021.105978.
[32] H. Cho, J. Chung, G. Shin, J.-Y. Sim, D.S. Kim, S. Lee, W. Hwang, Toward sustainable output generation of liquid–solid contact triboelectric nanogenerators: the role of hierarchical structures, Nano Energy 56 (2019) 56–64, https://doi.org/10.1016/j.nanoen.2018.11.039.
[33] S. Lee, E. Byeon, S. Jung, D.-G. Kim, Heterogeneity of hard skin layer in wrinkled PDMS surface fabricated by Ar ion-beam irradiation, Sci. Rep. 8 (2018) 14063, https://doi.org/10.1038/s41598-018-32378-2.
[34] S. Niu, Z.L. Wang, Theoretical systems of triboelectric nanogenerators, Nano Energy 14 (2015) 161–192, https://doi.org/10.1016/j.nanoen.2014.11.034.
[35] Y. Yang, H. Zhang, J. Chen, Q. Jing, Y.S. Zhou, X. Wen, Z.L. Wang, Single-electrode-based sliding triboelectric nanogenerator for self-powered displacement vector sensor system, ACS Nano 7 (2013) 7342, https://doi.org/10.1021/nn403021m.
[36] J. Chen, G. Zhu, W. Yang, Q. Jing, P. Bai, Y. Yang, T.-C. Hou, Z.L. Wang, Harmonic-resonator-based triboelectric nanogenerator as a sustainable power source and a self-powered active vibration sensor, Adv. Mater. 25 (2013) 6094, https://doi.org/10.1002/adma.201302397.
[37] P. Bai, G. Zhu, Z.-H. Lin, Q. Jing, J. Chen, G. Zhang, J. Ma, Z.L. Wang, Integrated multilayered triboelectric nanogenerator for harvesting biomechanical energy from human motions, ACS Nano 7 (2013) 3713, https://doi.org/10.1021/nn4007708.
[38] C.K. Jeong, K.M. Baek, S. Niu, T.W. Nam, Y.H. Hur, D.Y. Park, G.-T. Hwang, M. Byun, Z.L. Wang, Y.S. Jung, K.J. Lee, Topographically-designed triboelectric nanogenerator via block copolymer self-assembly, Nano Lett. 14 (2014) 7031, https://doi.org/10.1021/nl503402c.
[39] J.M. Wu, C.K. Chang, Y.T. Chang, High-output current density of the triboelectric nanogenerator made from recycling rice husks, Nano Energy 19 (2016) 39, https://doi.org/10.1016/j.nanoen.2015.11.014.
[40] Y. Kang, B. Wang, S. Dai, G. Liu, Y. Pu, C. Hu, Folded elastic strip-based triboelectric nanogenerator for harvesting human motion energy for multiple applications, ACS Appl. Mater. Interfaces 7 (2015) 20469, https://doi.org/10.1021/acsami.
[41] Z.-H. Lin, G. Cheng, X. Li, P.-K. Yang, X. Wen, Z.L. Wang, A multi-layered interdigitative-electrodes-based triboelectric nanogenerator for harvesting hydropower, Nano Energy 15 (2015) 256, https://doi.org/10.1016/j.nanoen.2015.04.037.
[42] B. Dudem, D.H. Kim, A.R. Mule, J.S. Yu, Enhanced performance of microarchitectured PTFE-based triboelectric nanogenerator via simple thermal imprinting lithography for self-powered electronics, ACS Appl. Mater. Interfaces 10 (2018) 24181, https://doi.org/10.1021/acsami.8b06295.
[43] P. Zhao, N. Soin, K. Prashanthi, J. Chen, S. Dong, E. Zhou, Z. Zhu, A.A. Narasimulu, C.D. Montemagno, L. Yu, J. Luo, Emulsion electrospinning of polytetrafluoroethylene (PTFE) nanofibrous membranes for high-performance triboelectric nanogenerators, ACS Appl. Mater. Interfaces 10 (2018) 5880, https://doi.org/10.1021/acsami.7b18442.
[44] H. Zhang, Y. Lu, A. Ghaffarinejad, P. Basseta, Progressive contact-separate triboelectric nanogenerator based on conductive polyurethane foam regulated with a Bennet doubler conditioning circuit, Nano Energy 51 (2018) 10, https://doi.org/10.1016/j.nanoen.2018.06.038.
[45] K. Xia, Z. Zhu, H. Zhang, C. Du, J. Fu, Z. Xu, Milk-based triboelectric nanogenerator on paper for harvesting energy from human body motion, Nano Energy 56 (2019) 400, https://doi.org/10.1016/j.nanoen.2018.11.071.
[46] Z. Zhang, Y. Xu, D. Wang, H. Yang, J. Guo, L.-S. Turng, Enhanced performance of an expanded polytetrafluoroethylene-based triboelectric nanogenerator for energy harvesting, Nano Energy 60 (2019) 903, https://doi.org/10.1016/j.nanoen.2019.04.034.
[47] K. Xia, D. Wu, J. Fu, N.A. Hoque, Y. Ye, Z. Xu, A high-output triboelectric nanogenerator based on nickel–copper bimetallic hydroxide nanowrinkles for self-powered wearable electronics, J. Mater. Chem. A 8 (2020) 25995, https://doi.org/10.1039/D0TA09440D.
[48] X. Zhang, A clover shaped triboelectric nanogenerator for self-powered grip strength test system, Mater. Technol. (2021), 1964216, https://doi.org/10.1080/10667857.2021.1964216.
[49] Z. Zhang, J. Cai, High output triboelectric nanogenerator based on PTFE and cotton for energy harvester and human motion sensor, Curr. Appl. Phys. 22 (2021) 1, https://doi.org/10.1016/j.cap.2020.11.001.
[50] Y. Zou, M. Sun, F. Yan, T. Du, Z. Xi, F. Li, C. Zhu, H. Wang, J. Zhao, P. Sun, M. Xu, A high-performance flag-type triboelectric nanogenerator for scavenging wind energy toward self-powered IoTs, Materials 15 (2022) 3696, https://doi.org/10.3390/ma15103696.
[51] Z.-H. Lin, Y. Xie, Y. Yang, S. Wang, G. Zhu, Z.L. Wang, Enhanced triboelectric nanogenerators and triboelectric nanosensor using chemically modified TiO_2 nanomaterials, ACS Nano 7 (2013) 4554, https://doi.org/10.1021/nn401256w.
[52] Z.H. Lin, G. Cheng, S. Lee, K.C. Pradel, Z.L. Wang, Harvesting water drop energy by a sequential contact-electrification and electrostatic-induction process, Adv. Mater. 26 (2014) 4690–4696, https://doi.org/10.1002/adma.201400373.
[53] Z.H. Lin, G. Cheng, L. Lin, S. Lee, Z.L. Wang, Water–solid surface contact electrification and its use for harvesting liquid-wave energy, Angew. Chem. Int. Ed. 52 (2013) 12545–12549, https://doi.org/10.1002/anie.201307249.
[54] Q. Liang, X. Yan, Y. Gu, K. Zhang, M. Liang, S. Lu, X. Zheng, Y. Zhang, Highly transparent triboelectric nanogenerator for harvesting water-related energy reinforced by antireflection coating, Sci. Rep. 5 (2015) 9080, https://doi.org/10.1038/srep09080.
[55] Y. Liu, N. Sun, J. Liu, Z. Wen, X. Sun, S.-T. Lee, B. Sun, Integrating a silicon solar cell with a triboelectric nanogenerator via a mutual electrode for harvesting energy from sunlight and raindrops, ACS Nano 12 (2018) 2893–2899, https://doi.org/10.1021/acsnano.8b00416.
[56] S.-B. Jeon, D. Kim, G.-W. Yoon, J.-B. Yoon, Y.-K. Choi, Self-cleaning hybrid energy harvester to generate power from raindrop and sunlight, Nano Energy 12 (2015) 636–645, https://doi.org/10.1016/j.nanoen.2015.01.039.
[57] S. Wang, Y. Xie, S. Niu, L. Lin, Z.L. Wang, Freestanding triboelectric-layer-based nanogenerators for harvesting energy from a moving object or human motion in contact and non-contact modes, Adv. Mater. 26 (2014) 2818–2824, https://doi.org/10.1002/adma.201305303.
[58] W. Zhang, G. Gu, H. Qin, S. Li, W. Shang, T. Wang, B. Zhang, P. Cui, J. Guo, F. Yang, G. Cheng, Z. Du, Measuring the actual voltage of a triboelectric nanogenerator using the non-grounded method, Nano Energy 77 (2020), 105108, https://doi.org/10.1016/j.nanoen.2020.105108.
[59] G. Shin, H. Yong, J. Chung, E. Cho, J. Ju, Z.-H. Lin, D. Kim, H. Lee, B. Koo, S. Lee, Condensed droplet-based electricity generation via water-phase change, Nano Energy 82 (2021), 105713, https://doi.org/10.1016/j.nanoen.2020.105713.
[60] S. Lin, L. Xu, A.C. Wang, Z.L. Wang, Quantifying electron-transfer in liquid-solid contact electrification and the formation of electric double-layer, Nat. Commun. 11 (2020) 399, https://doi.org/10.1038/s41467-019-14278-9.
[61] M. Sun, Q. Lu, Z.L. Wang, B. Huang, Understanding contact electrification at liquid–solid interfaces from surface electronic structure, Nat. Commun. 12 (2021) 1752, https://doi.org/10.1038/s41467-021-22005-6.
[62] H. Yong, S. Jung, D. Heo, W. Choi, J. Chung, S. Cho, P. Hwang, H. Song, W.-G. Koh, W. Lee, S. Lee, J. Hong, Body-mediated energy loss conversion for personalized cell vitalization, Nano Energy 87 (2021), 106209, https://doi.org/10.1016/j.nanoen.2021.106209.
[63] J. Li, Y. Dong, J.H. Park, J. Yoo, Body-coupled power transmission and energy harvesting, Nat. Electron. 4 (2021) 530–538, https://doi.org/10.1038/s41928-021-00592-y.
[64] H. Yong, D. Heo, B. Kim, H. Moon, K. Choi, D. Kim, S. Lee, Versatile energy loss conversion for recovering waste alternating potential through polarization transfer medium, Nano Energy 69 (2020), 104400, https://doi.org/10.1016/j.nanoen.2019.104400.
[65] T. Kim, H. Yong, B. Kim, D. Kim, D. Choi, Y.T. Park, S. Lee, Energy-loss return gate via liquid dielectric polarization, Nat. Commun. 9 (2018) 1437, https://doi.org/10.1038/s41467-018-03893-7.
[66] L. Yin, K.N. Kim, J. Lv, F. Tehrani, M. Lin, Z. Lin, J.-M. Moon, J. Ma, J. Yu, S. Xu, A self-sustainable wearable multi-modular E-textile bioenergy microgrid system, Nat. Commun. 12 (2021) 1542, https://doi.org/10.1038/s41467-021-21701-7.

Eunmi Cho is currently a Unified M.S and Ph.D. course student in the division of Materials Science & Engineering from Hanyang University, Seoul, Korea. She also is affiliated with Korea Research Institute of Chemical Technology (KRICT). She is studying functional thin film using fluoropolymer based materials under the supervisor of Dr. Sang-Jin Lee and Dr. Jin-Seong Park. Her main research interests include antireflective coating using sputtering process and thin-film for visible light region application.

Kyeong Nam Kim received his MS and Ph.D. degree in Materials Science and Engineering from Ulsan National Institute of Science and Technology (UNIST), Korea. He worked as post-doctoral fellow in the Department of Nanoengineering at University of California, San Diego (2018–2020) and was Young Scientist (YS) postdoctoral researcher at Korea Research Institute of Chemical Technology (2020–2022). And he is currently a senior researcher in the Division of Energy Technology at Daegu Gyeongbuk Institute of Science and Technology (DGIST), Korea. His research interests are on textile-based, printed energy-electronic devices for their integration into self-sustainable wearable system and multiarray patch.

Hyungseok Yong received his Ph.D. in Mechanical Engineering from Chung-Ang University in 2022. Now he works as postdoc in Chemical Materials Solutions Center from Korea Research Institute of Chemical Technology (KRICT). His main research interests focus on the fields of Energy harvester based on electrostatic potential, Triboelectric nanogenerator for energy harvesting device and self-powered sensor through electrostatic simulation, fluid dynamics analysis, and mechanism of energy loss conversion in electrical systems.

Woo Jin Choi is a principal researcher at Chemical Materials Solutions Center, KRICT. After his Ph.D. at Korea Advanced Institute of Science and Technology (KAIST, 2004), he was a researcher at GS Caltex and joined KRICT in 2009. His current research focuses on the mechanical properties of chemical materials and the construction of materials database (Chemical materials information bank, CMiB).

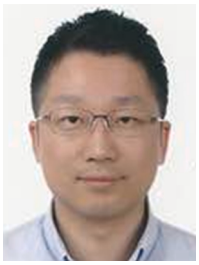

Jin-Seong Park is a professor at the Division of Materials Science & Engineering of Hanyang University, Seoul, Korea. His main research interests include the development of functional thin-film transistors and devices for flexible/transparent/wearable electronics. Before he joined the faculty of Hanyang University in 2013, he was a faculty member at the Department of Materials Science & Engineering of Dankook University, South Korea (2009–2013). He was also a senior researcher at Samsung SDI (2005–2008) and Samsung Mobile Display (2008–2009) as well as a post-doc fellow in the Department of Chemistry, Harvard University from 2003 to 2005.

Sang-Jin Lee received his Ph.D degree in physics from Pusan National University and has been a Principal Research Scientist at Chemical Materials Solutions Center of Korea Research Institute of Chemical Technology (KRICT) since 2012. He was a senior researcher at the LG Display R&D Center (2005–2007) as well as a research associate in the Department of Nanoengineering, University of California, San Diego (2019). His researches mainly focus the development of functional thin film using fluoropolymer based materials and also includes large-area electronic thin film materials by sputtering process.